European Polymer Journal 248 (2026) 114599

Contents lists available at ScienceDirect

European Polymer Journal

journal homepage: www.elsevier.com/locate/europolj

Pyrazine-tethered conjugated microporous polymers for silver nanoparticle dispersion toward enhanced catalytic reduction of *p*-nitrophenol and *p*-fluoronitrobenzene

Aya Osama Mousa [a], Mohamed Gamal Mohamed [a,b,*], Mohammed G. Kotp [a], Shiao-Wei Kuo [a,c,*]

[a] Department of Materials and Optoelectronic Science, Center for Functional Polymers and Supramolecular Materials, National Sun Yat-Sen University, Kaohsiung 804, Taiwan
[b] Chemistry Department, Faculty of Science, Assiut University, Assiut 71515, Egypt
[c] Department of Medicinal and Applied Chemistry, Kaohsiung Medical University, Kaohsiung 807, Taiwan

ARTICLE INFO

Keywords:
Pyrazine
Conjugated microporous polymers
Silver nanoparticles
In-situ metal reduction
Heterogeneous catalysis
Environmental remediation

ABSTRACT

Two pyrazine-based conjugated microporous polymers (CMPs), Py–PZ CMP and TPE–PZ CMP, were synthesized via Sonogashira–Hagihara coupling between 2-amino-3,5-dibromopyrazine (ADBPZ) and ethynyl-functionalized pyrene (PyT) or tetraphenylethylene (TPET) monomers. Both CMPs exhibit moderate porosity, high thermal stability, and distinct morphologies. Owing to the presence of amino-functionalized pyrazine nodes, the CMP frameworks enable the in situ reduction of Ag^{+} ions, resulting in uniformly dispersed silver nanoparticles without the need for external reducing agents. The resulting Ag@PZ-CMP composites were comprehensively characterized, confirming homogeneous silver distribution and preservation of the polymer framework. These Ag-decorated CMPs demonstrate efficient heterogeneous catalytic activity toward the reduction of nitro compounds, including *p*-nitrophenol (*p*-NP), following pseudo-first-order kinetics. The catalytic performance is strongly influenced by the polymer backbone and silver loading. Moreover, the catalysts exhibit good recyclability with minimal loss of activity over repeated cycles. Overall, this work presents an environmentally benign strategy for the rational design of robust and reusable Ag-based CMP catalysts.

1. Introduction

p-Nitrophenol (*p*-NP) is a toxic and persistent environmental pollutant frequently detected in industrial wastewater generated from dye manufacturing, pesticide production, and pharmaceutical processes [1–5]. Due to its high toxicity and poor biodegradability, *p*-NP poses severe risks to both human health and aquatic ecosystems [6]. Notably, Adsorptive removal of *p*-NP is primarily aimed at wastewater purification through physical separation, whereas the heterogeneous catalytic reduction pathway focuses on chemical transformation, which is even considered easier than photocatalytic degradation [7–9]. Transforming *p*-NP into its corresponding amino derivative, *p*-aminophenol (*p*-AP), not only significantly lowers its toxicity but also yields a high-value chemical widely applied in pharmaceuticals, benzoxazine resins, and synthetic dyes [10–15]. Heterogeneous catalysis offers an efficient and sustainable route for this conversion, enabling the rapid reduction of *p*-NP under mild reaction conditions, along with convenient catalyst separation, recovery, and reuse [16–18]. Consequently, the development of catalysts that are mechanically robust, chemically stable, and highly recyclable is essential for environmentally benign remediation technologies, particularly for the catalytic reduction of hazardous organic pollutants [16–21].

Covalent organic frameworks (COFs), polymers of intrinsic microporosity (PIMs), and conjugated micro- and *meso*-porous polymers (CMPs) are major members of porous organic polymers (POPs), a class of lightweight materials synthesized through precise organic coupling reactions [22–26]. Their architectures are pre-programmed through the rational design of monomers, enabling permanent, tunable pore networks with customizable surface chemistry [27]. POPs are extensively investigated in renewable energy systems, particularly as electronic

* Corresponding authors at: Department of Materials and Optoelectronic Science, Center for Functional Polymers and Supramolecular Materials, National Sun Yat-Sen University, Kaohsiung 804, Taiwan.
E-mail addresses: mgamal.eldin34@gmail.com, mgamal.eldin12@mail.nsysu.edu.tw (M.G. Mohamed), kuosw@faculty.nsysu.edu.tw (S.-W. Kuo).

https://doi.org/10.1016/j.eurpolymj.2026.114599
Received 11 January 2026; Received in revised form 12 February 2026; Accepted 20 February 2026
Available online 25 February 2026

platforms and robust supports for heterogeneous catalysts [28–30]. Compared with rigid inorganic pores (e.g., zeolites) and non-tunable porous carbons, POPs offer superior molecular-level design flexibility, allowing functional groups and metal-binding sites to be directly embedded into the polymer backbone [23]. This intrinsic tunability makes POPs promising, recyclable material platforms for sustainable energy conversion and environmental remediation. CMPs, a porous subclass of porous organic polymers (POPs), have garnered significant attention as an attractive support for heterogeneous catalysts due to their high surface area, adjustable pore architecture, chemical and thermal robustness, and highly π-conjugated frameworks [31–41]. CMPs could be readily functionalized with electron-rich ligating units, particularly amino groups, which effectively coordinate and immobilize metal nanoparticles, suppress nanoparticle coalescence, prevent aggregation, and promote interfacial electron transfer, ultimately leading to enhanced catalytic efficiency [42–44]. The integration of CMP porosity with metal nanoparticle decoration enables the construction of heterogeneous catalysts that exhibit both high activity and recyclability across a broad spectrum of reduction reactions [45,46]. Although silver-decorated CMPs (Ag@CMPs) have demonstrated strong potential in catalytic pollutant remediation and reduction chemistry, many reported systems still encounter persistent challenges, including insufficient and non-simple metal loading, non-uniform nanoparticle distribution, and particle aggregation, all of which restrict catalytic performance and long-term recyclability [47–50]. Among nitrogen-rich building units, pyrazine (PZ) stands out as a structurally advantageous yet underutilized node for CMP design. Pyrazine-based CMPs offer a rigid, planar backbone and electron-donating nitrogen coordination centers capable of strongly anchoring and stabilizing metal nanoparticles with high spatial control [51–55]. Despite these intrinsic benefits, pyrazine (PZ)-derived CMPs remain rarely investigated as support for Ag nanoparticles in catalytic reduction reactions. The development of Ag-loaded PZ-based CMP catalysts could provide a strategic pathway to resolve existing limitations in Ag@CMP materials, enabling higher metal dispersion, more accessible active interfaces, improved reduction kinetics, and superior catalyst recyclability. Such systems would advance the design of durable, high-loading, and anti-aggregation polymeric catalyst platforms for sustainable reduction chemistry and environmental detoxification.

Herein, we report the rational design, synthesis, and comprehensive characterization of two new pyrazine-based CMP-Py-PZ CMP and TPE-PZ CMP-constructed through a Pd(0)-catalyzed Sonogashira–Hagihara cross-coupling reaction [Fig. 1]. The pendant nitrogen atoms and amino groups within the PZ-CMP frameworks enable the in-situ reduction of Ag^{+}, producing uniformly and highly dispersed silver nanoparticles without the need for external reducing agents or additives [56,57]. The as-formed Ag@PZ-CMP nanocomposites were investigated as recyclable heterogeneous catalysts and demonstrated excellent catalytic efficiency toward the reduction of multiple nitro-containing substrates, including *p*-nitrophenol (*p*-NP) and *p*-fluoronitrobenzene (*p*-FNB) derivatives. The

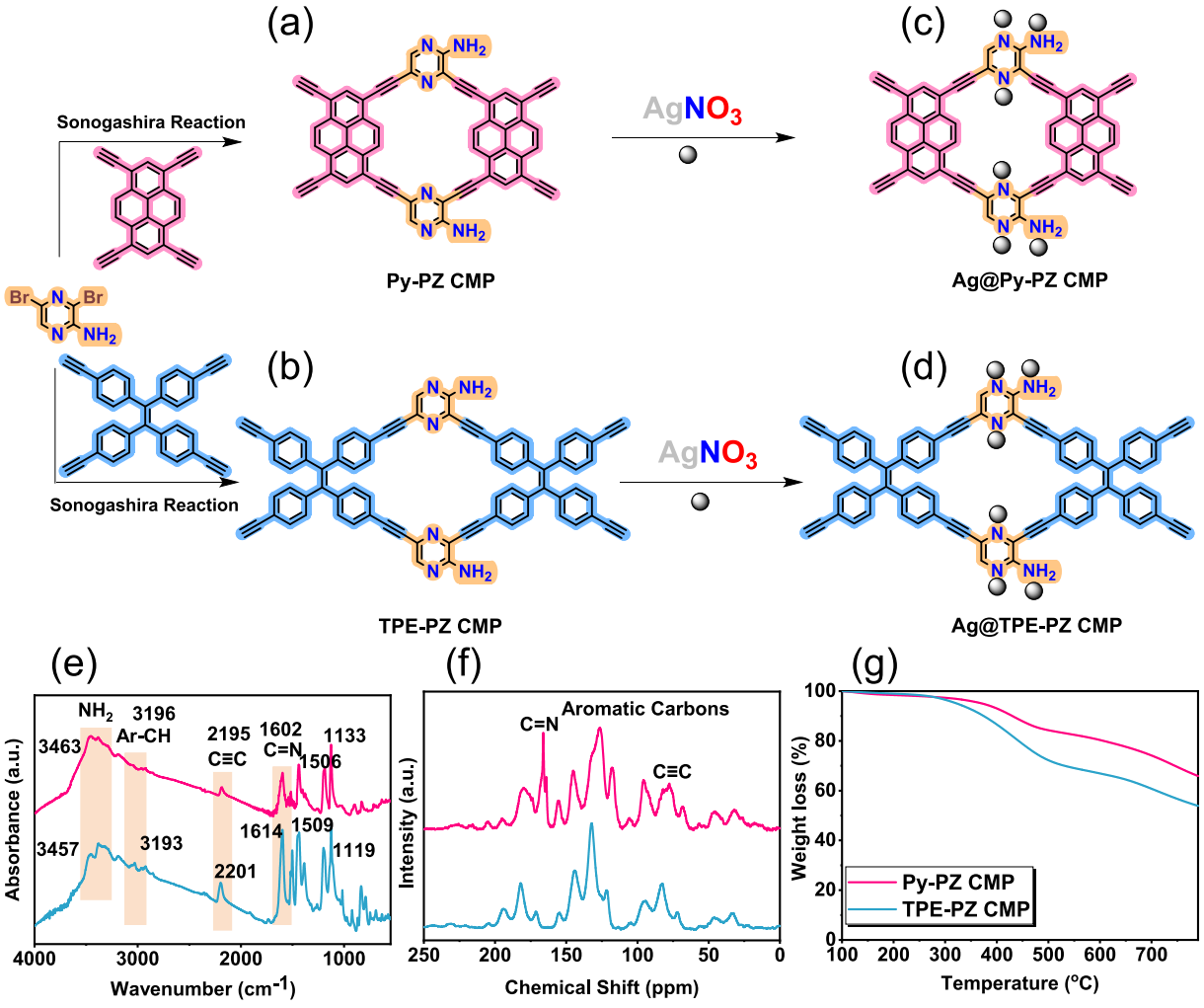

Fig. 1. Synthesis protocol of (a) Py-PZ CMP and (b) TPE-PZ CMP and the corresponding (c) Ag@Py-PZ CMP and (d) Ag@TPE-PZ CMP. (e) FTIR, (f) solid state ^{13}C NMR, and (g) TGA profiles of Py-PZ and TPE-PZ CMPs.

synergistic integration of microporous channels, stable polymer scaffold, and homogeneously distributed Ag nanoparticles affords catalyst systems with tunable reactivity, strong structural durability, and high recyclability, offering practical potential for a wide range of environmentally significant mild reduction transformations.

2. Experimental section

2.1. Materials

Triphenylphosphine (PPh_3, 99%), acetone, copper(I) iodide (CuI, 98%), methanol (MeOH), dimethylformamide (DMF), triethylamine (Et_3N, 99.5%), silver nitrate ($AgNO_3$, crystals), tetrahydrofuran (THF), *p*-nitrophenol (*p*-NP) and *p*-fluoronitrobenzene (*p*-FNB), 2-amino-3,5-dibromopyrazine (ADBPZ), and tetrakis(triphenylphosphine)palladium (0) [$Pd(PPh_3)_4$] were purchased from Thermo Scientific and Alfa Aesar and used as received. The pyrene-based monomer 1,3,6,8-tetraethynylpyrene (PyT) and the tetraphenylethene derivative 1,1,2,2-tetrakis(4-ethynylphenyl)ethene (TPET) were synthesized and fully characterized in our previous studies [58,59].

2.2. Synthesis of Py-PZ CMP and TPE-PZ CMP

PyT (500 mg, 1.675 mmol), ADBPZ (840 mg, 3.32 mmol), PPh_3 (40 mg, 0.153 mmol), CuI (30 mg, 0.158 mmol), and $Pd(PPh_3)_4$ (190 mg, 0.164 mmol) were added to a mixture of DMF (7.5 mL) and Et_3N (7.5 mL). The reaction mixture was degassed using three freeze–pump–thaw cycles under a nitrogen atmosphere and sealed in a Schlenk tube. The polymerization was conducted at 115 °C for 72 h under magnetic stirring. After completion, the mixture was cooled to room temperature, filtered, and thoroughly washed with THF, acetone, water, and methanol. The resulting solid was dried under vacuum to afford Py-PZ CMP as a dark brown solid [FTIR: 3463, 3196, 2195, 1602, 1506, 1133, 3463 cm^{-1}]. The synthesis of TPE-PZ CMP followed the same procedure described for Py-PZ CMP. TPET (500 mg, 1.167 mmol), ADBPZ (590 mg, 2.33 mmol), PPh_3 (30 mg, 0.11 mmol), CuI (20 mg, 0.10 mmol), and $Pd(PPh_3)_4$ (130 mg, 0.112 mmol) to obtain TPE-PZ CMP as an orange powder [FTIR: 3457, 3193, 2201, 1614, 1509, 1119 cm^{-1}].

2.3. Synthesis of Ag@Py-PZ CMP and Ag@TPE-PZ CMP nanocatalysts

Ag-decorated CMPs were prepared by dispersing 10 mg of the corresponding PZ-based CMP in 10 mL of an aqueous $AgNO_3$ solution (1 and 3 mmol L^{-1}). The mixtures were magnetically stirred for 24 h to allow in-situ reduction and deposition of silver species onto the polymer frameworks. The resulting composites were isolated by centrifugation, washed three times with distilled water and methanol, and dried at 50 °C. This procedure afforded *x*Ag@Py-PZ CMP as a brown solid and *x*Ag@TPE-PZ CMP as a dark orange solid.

2.4. Procedure for the reduction of p-NP to p-AP

The catalytic reduction of *p*-NP was carried out by first mixing freshly prepared $NaBH_4$ solution (0.5 mL, 0.08 M) with an aqueous p-nitrophenol solution (2.0 mL, 0.16 mM) in a quartz cuvette, resulting in the characteristic deep yellow colour associated with the formation of p-nitrophenolate ions. Subsequently, 0.5 mL of Ag@Py-PZ CMP or Ag@TPE-PZ CMP solution (1 mg mL^{-1}) was added to initiate the reaction. Upon catalyst introduction, the yellow coloration progressively faded as the reduction proceeded. The reaction progress was monitored in real time using UV–vis spectroscopy by following the decrease of the absorption band at 400 nm and the concurrent appearance of the product band near 300 nm.

2.5. Recyclability of Ag@Py-PZ CMP and Ag@TPE-PZ CMP

After each catalytic reduction of *p*-NP to *p*-AP, the Ag@Py-PZ CMP and Ag@TPE-PZ CMP catalysts were recovered by centrifugation, followed by thorough washing with water and ethanol. The catalysts were then dried and reused for up to five consecutive cycles to evaluate their recyclability and operational stability. After each run, the recovered materials were carefully handled to minimize mass loss before being reintroduced into the reaction. Following the fifth cycle, both Ag@Py-PZ CMP and Ag@TPE-PZ CMP were characterized by FTIR to assess any compositional changes during repeated use.

3. Results and discussion

3.1. Synthesis and characterization of Py-PZ CMP and TPE-PZ CMP

In this work, two CMPs, Py-PZ CMP and TPE-PZ CMP, were successfully synthesized through a straightforward approach based on Pd (0)-catalyzed Sonogashira–Hagihara cross-coupling polymerization between 2-amino-3,5-dibromopyrazine (ADBPZ) and Py- or TPE-based monomers [Fig. 1(a) and (b)]. The resulting two CMPs were isolated in high yields and comprehensively characterized to verify their chemical structures, porosity, and optical properties. Benefiting from the electron-rich $–NH_2$ groups within the pyrazine (PZ) nodes and the extended π-conjugated polymer backbone, both CMPs demonstrated an intrinsic ability to reduce Ag^+ ions in situ, leading to the formation of uniformly dispersed silver nanoparticles on their surfaces without the use of any external reducing agents. The obtained Ag@Py-PZ CMP and Ag@TPE-PZ CMP composites [Fig. 1(c) and (d)] were subsequently investigated as heterogeneous catalysts for the model reduction of nitroaryl molecules into less hazardous amino derivatives. The following sections provide a detailed discussion of CMP structural characterization, the formation and stabilization of anchored Ag nanoparticles, and the catalytic performance of the Ag-decorated polymers, with a focus on the key structure–property relationships that govern catalytic activity.

The FTIR spectra of the PZ-based CMPs display the characteristic vibrational features expected for extended π-conjugated frameworks [Fig. 1(e)]. The aromatic C–H stretching mode is observed at 3196 cm^{-1} and 3193 $cm^{-1,}$ respectively for Py-PZ CMP and TPE-PZ CMP, while the sharp band at 2195 cm^{-1} and 2201 $cm^{-1,}$ respectively for Py-PZ CMP and TPE-PZ CMP are attributed to the alkyne (–C≡C–) stretching vibration, confirming the successful incorporation of ethynyl linkers through Sonogashira coupling [58–60]. The signals at 1602 and 1506 cm^{-1} and 1614 and 1509 $cm^{-1,}$ respectively, for Py-PZ CMP and TPE-PZ CMP, correspond to the C═N and C═C stretching vibrations, respectively, in agreement with the presence of the pyrazine core and the conjugated aromatic polymer backbone. In addition, the bands at 1133 cm^{-1} and 1119 $cm^{-1,}$ respectively for Py-PZ CMP and TPE-PZ CMP, are assigned to C–N stretching, further supporting the formation of a pyrazine-integrated polymer network. A broad absorption centered at 3463 cm^{-1} is associated with physically adsorbed water molecules trapped within the microporous structure, a feature commonly reported for conjugated microporous and other microporous organic polymers. Taken together, these FTIR signatures provide strong evidence for the successful construction of the designed PZ-based CMP frameworks. The solid-state ^{13}C NMR spectra provide additional evidence for the successful construction of the PZ-based CMP frameworks [Figs. 1(f) and S1]. The broad resonances in the 115–144 ppm region are characteristic of aromatic carbon environments within the extended π-conjugated backbone. Two distinguishable peaks at 166 ppm and 148 ppm are assigned to the C═N and C–N carbons of the pyrazine units, respectively, verifying their incorporation into the polymer network. Furthermore, the signals detected in the 85–73 ppm range correspond to the sp-hybridized internal carbons of the C≡C linkages, indicating that the alkyne linkers were effectively preserved during Sonogashira-Hagihara coupling between ADBPZ and the ethynyl Py- or TPE-based

monomers. Collectively, these spectral features confirm the formation of the targeted, cross-linked, PZ-tethered CMPs. The thermal properties of the PZ-based CMPs were investigated by thermogravimetric analysis (TGA) under a nitrogen atmosphere up to 800 °C. Both Py-PZ CMP and TPE-PZ CMP demonstrated excellent thermal stability, exhibiting 10% weight-loss temperatures (T_{d10}) of 430 °C and 366.5 °C, respectively, which confirms the robustness of their cross-linked polymer networks [Fig. 1(g)]. At 800 °C, the char yields remained high-65.8% for Py-PZ CMP and 53.8% for TPE-PZ CMP, indicating strong thermal resistance and a high carbon content in both frameworks. The superior T_{d10} and char yield of Py-PZ CMP are attributed to its rigid, highly planar pyrene-based backbone, which provides enhanced structural stability compared with the more flexible TPE-based network. These findings verify that both CMPs possess high thermal robustness, making them promising candidates for applications that require resilience under elevated temperatures.

X-ray photoelectron spectroscopy (XPS) was performed on the pristine PZ-based CMPs to analyze the elemental composition and the bonding environments of carbon and nitrogen atoms. The C 1s spectrum of Py-PZ CMP displays three dominant peaks at 283.76, 284.93, and 285.85 eV, representing distinct carbon chemical states within the polymer network [Fig. 2(a)]. The peak at 283.76 eV (FWHM = 1.39 eV, area = 13872.6) is assigned to aromatic C–C/C═C species in the pyrene and pyrazine rings. The 284.93 eV peak (FWHM = 1.11 eV, area = 3760.9) corresponds to sp^2 carbons bonded to nitrogen (C–N), while the 285.85 eV peak (FWHM = 1.08 eV, area = 1976) is attributed to carbons neighboring electron-withdrawing functionalities. Likewise, TPE-PZ CMP exhibits C 1s peaks at the same binding energy, with integrated areas of 7081, 3930, and 2625, respectively [Fig. 2(a)], indicating a similar distribution of carbon environments in the TPE-linked framework. The well-resolved convolution of these signals confirms the successful integration of pyrazine nodes and ethynyl-based linkers in both CMP architectures, in agreement with the designed polymer structures. To further probe nitrogen chemistry, high-resolution N 1s XPS analysis was carried out for both Py-PZ CMP and TPE-PZ CMP [Fig. 2(b)]. The N 1s spectra of the two polymers can be reliably deconvoluted into two principal components centered at ~ 398.85 eV and ~ 398.13 eV, which are assigned to C-N and C═N species within the pyrazine heterocycles, respectively. The presence of these signals verifies the successful incorporation of pyrazine building blocks into the CMP frameworks. The similar binding energies and narrow FWHM values observed for both materials suggest high chemical stability and a uniform distribution of nitrogen sites throughout the polymer networks. Table S1 summarizes fitting parameters of HRXPS signals for C 1s, N 1s, and Ag 3d resulting from Py-PZ CMP and TPE-PZ CMP. The porosity of the synthesized PZ-based CMPs was examined through nitrogen adsorption–desorption measurements at 77 K. The isotherms of Py-PZ CMP and TPE-PZ CMP [Fig. 2(c) and (d)] show a steady rise in gas uptake at low relative pressures, followed by a sharp increase as the pressure approaches $P/P_0 \approx 1$.

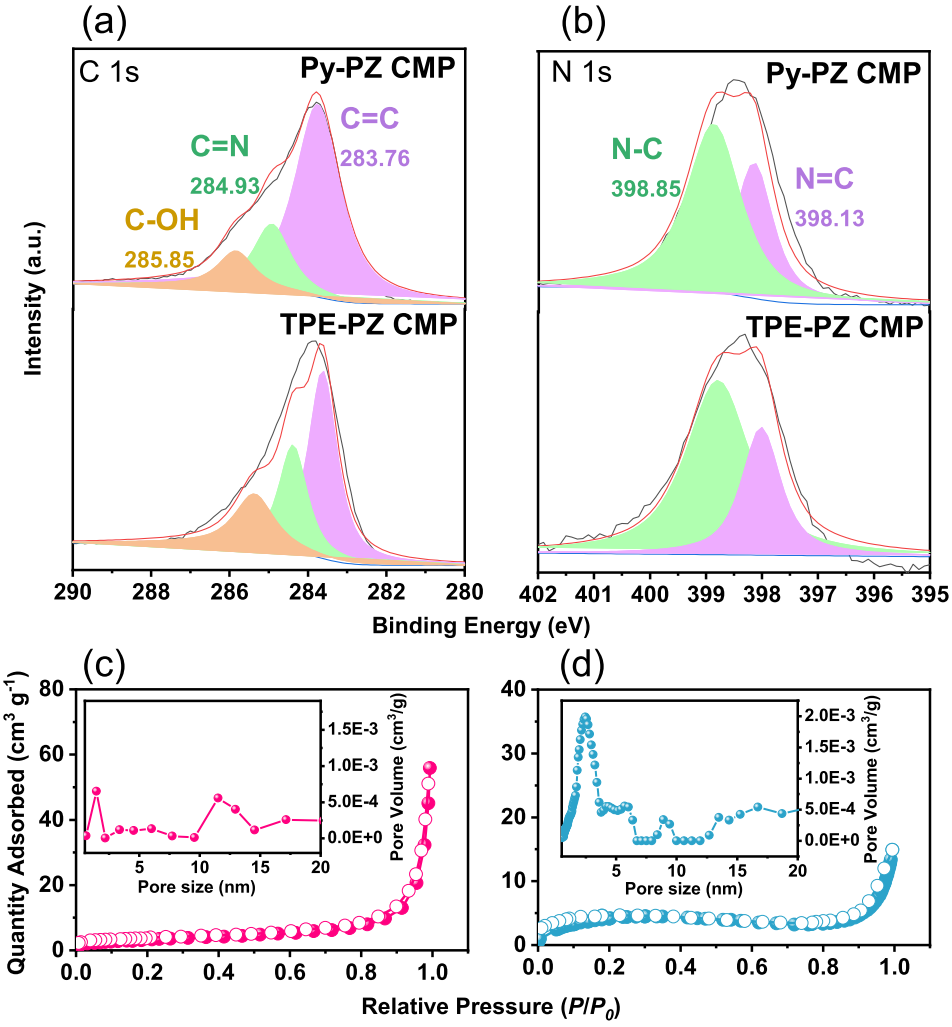

Fig. 2. High-resolution X-ray photoelectron spectroscopy (HRXPS) spectra of (a) C 1s and (b) N 1s for Py-PZ and TPE-PZ CMPs. Nitrogen adsorption–desorption isotherms of (c) Py-PZ CMP and (d) TPE-PZ CMP. Insets in Fig. 2(c) and 2(d) show the corresponding pore size distribution curves of the Py-PZ and TPE-PZ CMPs.

This adsorption behavior confirms the formation of a combined micro- to mesoporous framework. The Brunauer-Emmett-Teller (BET) surface areas were calculated to be 13 m^2 g^{-1} for Py-PZ CMP and 5 m^2 g^{-1} for TPE-PZ CMP. The pore size distributions derived using density functional theory (DFT) analysis based on the adsorption data [Fig. 2(c) and (d)], further reveal a hierarchical pore system in both polymers. Py-PZ CMP exhibits characteristic pore widths centered at 2.37, 5.85, and 9.10 nm, while TPE-PZ CMP displays pores at 1.36, 6.33, and 11.67 nm [inset Fig. 2(c) and (d)]. These features are more relevant to mass transport and exposure of Ag nanoparticles during catalysis. In the present PZ-based CMPs, the rigid pyrazine nodes combined with bulky Py or TPE linkers lead to irregular packing and non-uniform network growth, which can generate interstitial voids and textural mesopores in addition to intrinsic micropores. Furthermore, the aggregation of polymer particles during polymerization and drying can create interparticle mesoporosity, which is commonly observed in CMP systems. Therefore, the coexistence of micro- and mesopores in the pore size distribution reflects the realistic structural organization of the CMPs rather than a discrepancy, and this hierarchical porosity is advantageous for mass transport in catalytic applications. The relatively higher BET surface area and smaller dominant micropore size of Py-PZ CMP can be attributed to its rigid and planar pyrene-based backbone, which promotes a more defined porous network compared with the more flexible TPE-linked framework. The FTIR spectra of Ag@Py-PZ CMP and Ag@TPE-PZ CMP retain the key vibrational bands of the pristine Py-PZ CMP and TPE-PZ CMP [Fig. S2], confirming that the overall chemical framework remains intact after silver loading. However, slight but consistent shifts in several diagnostic peaks indicate interactions between the polymer network and the in-situ-generated Ag nanoparticles [61,62]. For instance, the broad N–H stretching band shifts from 3457 to 3450 cm^{-1}, while the C═N/C═C stretching band moves from 1593 to 1600 cm^{-1} after silver deposition. These subtle shifts suggest that the electron-rich $–NH_2$ groups and nitrogen sites within the pyrazine (PZ) rings interact with Ag^+ ions during the reduction process, serving both as intrinsic reducing centers and coordination sites that stabilize the resulting Ag^0 nanoparticles. The observed blue shift toward higher wavenumbers further reflects a slight perturbation of the local electronic environment around the amino and C═N units upon metal coordination, supporting the proposed mechanism in which the $–NH_2$-functionalized pyrazine nodes enable external-reagent-free reduction of Ag^+ to metallic Ag^0. More detailed analysis of the C 1s XPS spectra of Ag-loaded CMPs reveals three dominant components at 283.76, 284.93, and 285.85 eV, assigned to aromatic C–C/C═C, C–N bonds, and carbons adjacent to electron-withdrawing groups, respectively [Fig. 3(a)]. The binding energies remain nearly identical to those of the pristine CMPs, confirming that the conjugated polymer backbone is retained after Ag deposition. Despite this, clear differences in peak intensities and integrated areas emerge most prominently in the C–N contribution. Ag@Py-PZ CMP exhibits an increased C–N peak area, implying a stronger interaction between nitrogen-rich sites and anchored Ag nanoparticles, whereas Ag@TPE-PZ CMP shows a comparatively larger aromatic C–C/C═C contribution, reflecting the distinct structural and electronic environments of the two frameworks. The N 1s spectra offer more direct evidence of Ag–nitrogen interactions [Fig. 3(b)]. Two components centered at 398.85 eV and 398.13 eV are observed in both Ag-coated CMPs, corresponding to C-N and C═N, respectively. Following Ag loading, the overall N 1s peak areas decrease relative to the pristine materials, indicating partial coordination between Ag nanoparticles and nitrogen sites, particularly at amine groups, which have been proposed to facilitate the in-situ reduction of Ag^+ to Ag^0 [63]. The subtle changes in nitrogen binding environments are further supported by FTIR results, where slight blue shifts in N–H and C═N stretching modes were detected after Ag incorporation, suggesting modification of the local bonding environment without disrupting the original framework. The formation of metallic Ag nanoparticles is confirmed by the well-resolved Ag $3d^{5/2}$ and Ag $3d^{3/2}$ peaks at 368.17 eV and 374.19 eV [Fig. 3(c)].

The narrow full-width at half maximum (FWHM) values verify the presence of well-defined Ag^0 species. Notably, Ag@Py-PZ CMP displays a larger Ag 3d peak area than Ag@TPE-PZ CMP, indicating that the Py-PZ CMP incorporates or stabilizes a higher quantity of Ag nanoparticles. This result is consistent with the rigid, planar pyrene backbone, which likely exposes more accessible nitrogen coordination sites for reducing and anchoring Ag ions. In contrast, the more sterically hindered and flexible TPE-based network interacts with a slightly lower Ag content, leading to a reduced Ag 3d signal intensity. ICP analysis was performed to quantify the amount of Ag incorporated into the PZ-CMPs prepared using two $AgNO_3$ concentrations (1 and 3 mmol L^{-1}). The results indicate that the Py-PZ CMP incorporates slightly more silver than the TPE-PZ CMP under identical preparation conditions. For Py-PZ CMP, the samples obtained from $AgNO_3$ solutions (1 and 3 mmol L^{-1}) exhibit Ag loadings of 0.57 wt% and 0.91 wt%, respectively, demonstrating that higher Ag precursor concentrations lead to a proportional increase in

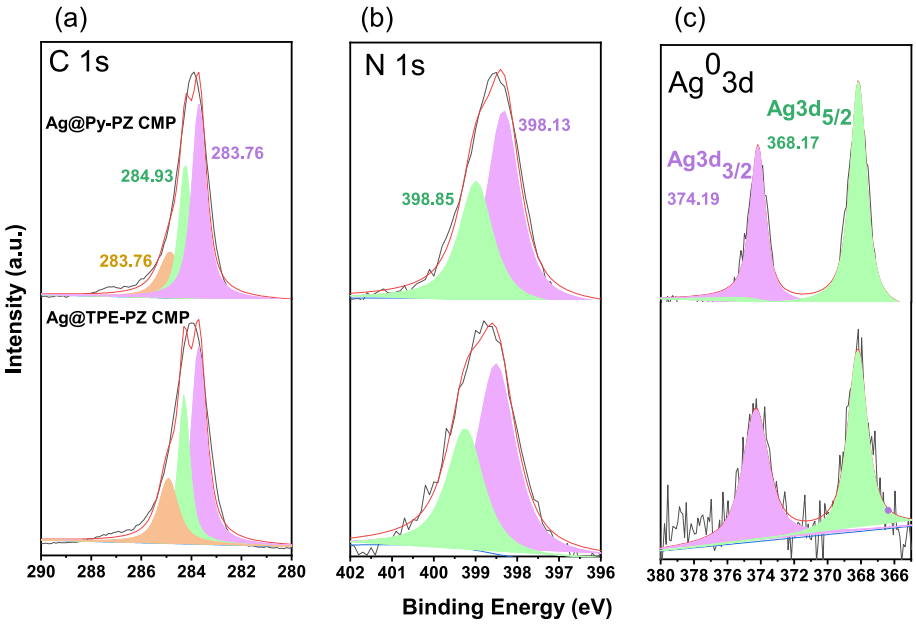

Fig. 3. (a–c) HRXPS spectra of (a) C, (b) N, and (c) Ag for Ag@Py-PZ and Ag@TPE-PZ CMPs.

silver incorporation. Similarly, the TPE-PZ CMP samples contain 0.29 wt % (1 mmol L^{-1}) and 0.71 wt% (3 mmol L^{-1}) Ag, confirming successful silver uptake, albeit at consistently lower levels than in the Py-PZ CMP sample. Notably, every ICP measurement was conducted in triplicate, and the relative standard deviations (RSDs) were below 2%, confirming the good reproducibility and reliability of the quantified Ag loadings.

To further assess the effect of Ag nanoparticle incorporation, the thermal stability of Ag@Py-PZ CMP and Ag@TPE-PZ CMP was also examined. The Ag-loaded composites maintained high thermal resistance, with T_{d10} values of 373.3 °C for Ag@Py-PZ CMP and 387.99 °C for Ag@TPE-PZ CMP (Fig. S3). Notably, the introduction of Ag nanoparticles did not weaken the structural integrity of the CMP networks. On the contrary, Ag slightly improved thermal resistance, likely by restricting polymer chain mobility and facilitating more efficient heat dissipation. The composites also retained considerable carbonized residues at 800 °C, yielding 50.77% for Ag@Py-PZ CMP and 56.87% for Ag@TPE-PZ CMP. The morphologies of the synthesized PZ-CMPs were analyzed by scanning electron microscopy (SEM). Py-PZ CMP exhibits a thin, sheet-like architecture, which aligns with its rigid and planar pyrene-based backbone that favors π–π stacking, interlayer assembly, and extended surface exposure [Fig. 4(a)]. In contrast, TPE-PZ CMP displays a uniform spherical morphology [Fig. 4(b)], arising from the flexible and non-planar configuration of the TPE-derived monomer. The pronounced difference in particle shape suggests that the molecular geometry and rigidity of the polymer backbone significantly influence network packing and the final CMP morphology, which may impact guest-molecule diffusion pathways and catalytic accessibility. The Py-PZ CMP exhibits relatively smaller and more uniformly distributed pores and a sheet-like morphology compared to the spherical TPE-PZ CMP. These features are more relevant to mass transport and exposure of Ag nanoparticles during catalysis than the absolute BET value. To evaluate the impact of silver incorporation, the morphologies of Ag@Py-PZ CMP and Ag@TPE-PZ CMP were further examined after in-situ Ag nanoparticle deposition. Both composites preserve the characteristic shapes of their pristine polymer networks. Ag@Py-PZ CMP maintains its ultrathin sheet-like layers [Fig. 4(c)], while Ag@TPE-PZ CMP retains its monodisperse spherical particles [Fig. 4(d)]. In addition, the SEM images reveal bright, nanosized contrast features homogeneously distributed across the polymer surfaces.

These high-contrast spots are attributed to Ag nanoparticles, whose greater electron density produces a stronger signal contrast under SEM imaging. The consistent appearance of Ag-rich domains across both sheets and spheres verifies the successful formation and uniform dispersion of silver nanoparticles throughout each CMP network. The retention of the original CMP morphologies, together with the presence of well-distributed Ag nanoparticles, demonstrates that the in-situ reduction process effectively anchors and stabilizes Ag within the porous polymer frameworks without compromising structural integrity. Elemental mapping analysis was conducted on Ag@Py-PZ CMP [Fig. 4(e)] and Ag@TPE-PZ CMP [Fig. 4(f)] to visualize the spatial distribution of the primary elements (C, N, and Ag) within the composites. The carbon and nitrogen signals, derived from the polymer backbone and PZ units, exhibit a homogeneous distribution across the entire surfaces of both CMPs, confirming the structural uniformity of the organic frameworks. Notably, the silver maps also reveal an even dispersion of Ag throughout the layered, sheet-like Py-PZ network and the spherical TPE-PZ particles. This consistent distribution demonstrates that the in-situ reduction process successfully generates well-dispersed silver nanoparticles, avoiding the formation of large, aggregated clusters. Furthermore, the strong spatial overlap among the C, N, and Ag regions suggests that the nitrogen- and amine-rich coordination sites within the CMP frameworks play a crucial role in anchoring the Ag nanoparticles, promoting stable immobilization within the polymer matrices. TEM images provide further evidence supporting the SEM observations. The Py-PZ CMP displays ultrathin, sheet-like layers [Fig. 4(g)], which align with its planar, pyrene-based backbone structure. In contrast, the TPE-PZ CMP exhibits well-defined spherical nanoparticles [Fig. 4(h)], reflecting the non-planar geometry of the TPE backbone. Importantly, TEM analysis also confirms that both CMPs possess interconnected porous internal networks, a structural feature that is critical for efficient guest-molecule diffusion and beneficial for catalytic applications. TEM characterization was also performed on the Ag-loaded PZ-CMPs to

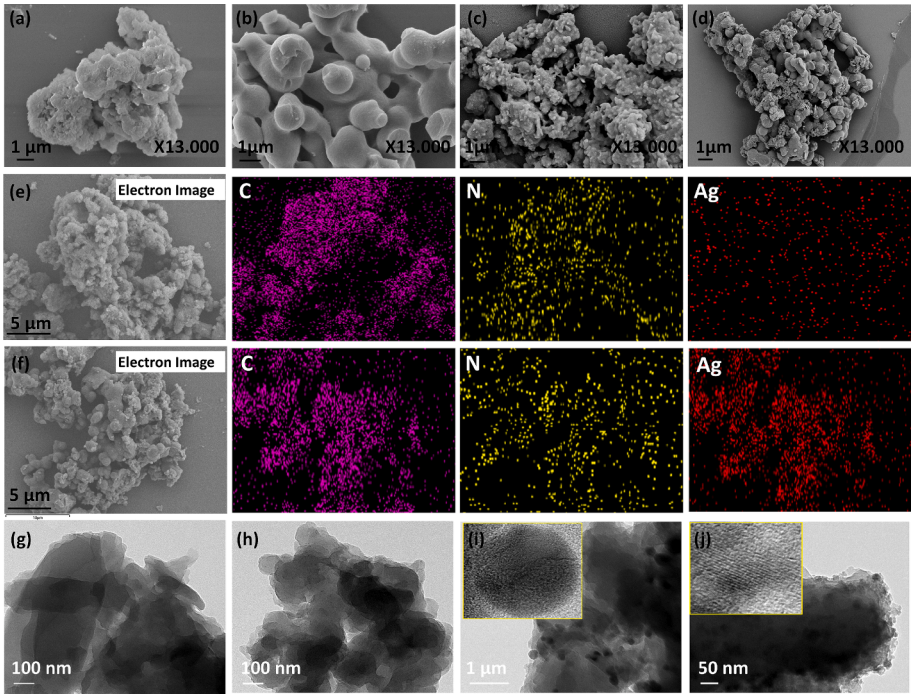

Fig. 4. (a–d) SEM images of (a) Py-PZ CMP, (b) TPE-PZ CMP, (c) Ag@Py-PZ CMP, and (d) Ag@TPE-PZ CMP. (e, f) SEM-EDS elemental mapping images showing the homogeneous distribution of C, N, and Ag in (e) Ag@Py-PZ CMP and (f) Ag@TPE-PZ CMP. (g-j) TEM images of (g) Py-PZ CMP, (h) TPE-PZ CMP, (i) Ag@Py-PZ CMP, and (j) Ag@TPE-PZ CMP. The inset TEM images in (i) and (j) reveal the crystalline features of Ag nanoparticles embedded within the CMP frameworks.

investigate the internal morphology and verify the presence and spatial distribution of silver nanoparticles. Consistent with SEM results, Ag@Py-PZ CMP retains its layered, sheet-like domains [Fig. 4(i)], while Ag@TPE-PZ CMP preserves its spherical particle morphology [Fig. 4(j)], indicating that the polymer architectures remain structurally intact after silver incorporation. Both samples reveal abundant dark, high-contrast dots uniformly distributed across the CMP surfaces. These features correspond to metallic Ag nanoparticles, as silver exhibits significantly higher electron density than the organic polymer matrix, resulting in darker contrast under TEM. The homogeneous dispersion of these nanoparticles demonstrates the success of the in-situ reduction process in generating well-distributed nanosized Ag particles within the CMP frameworks. Collectively, the TEM results confirm the preservation of the native PZ-CMPs morphologies and the effective deposition of finely dispersed Ag nanoparticles throughout the PZ-CMPs networks. The lattice fringes observed in the high-resolution TEM images [Fig. 4(i) and (j)] exhibit an interplanar spacing of approximately ~ 0.23–0.24 nm, which can be indexed to the (1 1 1) plane of face-centered cubic (FCC) metallic silver. Furthermore, we have conducted a statistical analysis using multiple TEM images and added a particle size distribution histogram based on measurements of more than 100 nanoparticles (Fig. S4). The results show a narrow size distribution with an average diameter of ~ 3–9 nm, indicating uniform dispersion and effective confinement of Ag nanoparticles within CMPs matrix. Powder XRD measurements were performed for both Ag@Py-PZ CMP and Ag@TPE-PZ CMP (Fig. S5). Distinct diffraction peaks were observed at 2θ ≈ 38.09°, 44.10°, and 64.34°, which can be indexed to the (1 1 1), (200), and (220) planes of face-centered cubic (fcc) metallic silver. These reflections confirm the successful reduction of Ag^{+} to crystalline Ag^{0} nanoparticles within the CMP frameworks. The relatively weak peak intensities are consistent with the low Ag loading and the small nanoparticle size, as well as the predominantly amorphous nature of the polymer matrix.

3.2. Catalytic performance of Ag@Py-PZ CMP and Ag@TPE-PZ CMP

The catalytic performance of Ag-decorated PZ-CMPs was evaluated through the reduction of *p*-nitrophenol (*p*-NP) to *p*-aminophenol (p-AP) using sodium borohydride ($NaBH_4$) as the reducing agent. After the addition of Ag@PZ-CMP catalysts, the characteristic UV–Vis absorption peak of *p*-NP at 400 nm gradually diminished, while a new peak at approximately 300 nm emerged, corresponding to the formation of the amino product. This spectral evolution confirms successful catalytic conversion, as shown in Fig. 5(a–d). A comparison across catalysts reveals that the reduction rate is strongly dependent on both the Ag loading and the polymer backbone. In the Py-PZ CMP series, 3Ag@Py-PZ CMP [Fig. 5(a)] demonstrated markedly faster conversion than 1Ag@Py-PZ CMP [Fig. 5(b)], indicating that increased silver content enhances catalytic activity by supplying a greater number of active sites to facilitate electron transfer. A consistent trend was also observed in the TPE-PZ CMP series, where 3Ag@TPE-PZ CMP [Fig. 5(c)] achieved a more rapid reduction of *p*-NP compared with 1Ag@TPE-PZ CMP [Fig. 5 (d)]. Furthermore, the Py-PZ CMP-based catalysts consistently outperform their TPE-PZ CMP-based counterparts at comparable Ag loadings. For instance, 1Ag@Py-PZ CMP achieves complete reduction in a shorter time than 1Ag@TPE-PZ CMP, while 3Ag@Py-PZ CMP also exhibits

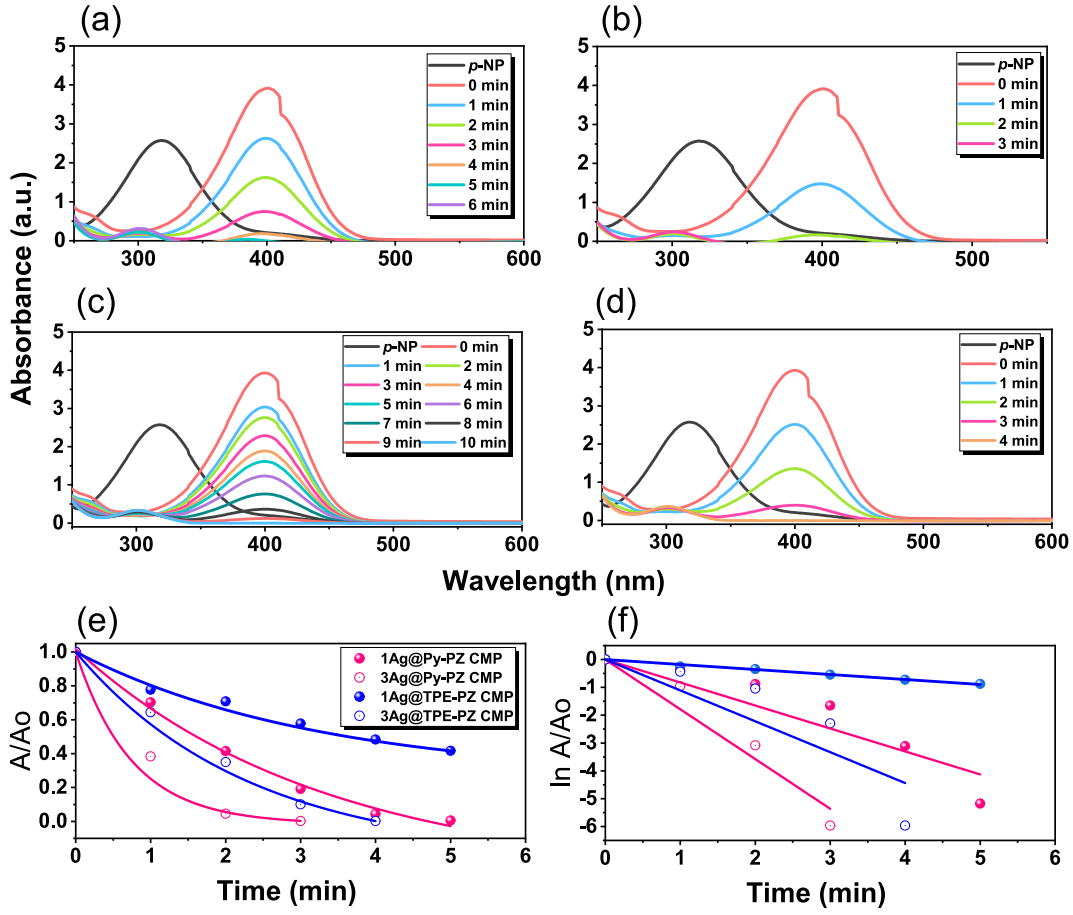

Fig. 5. UV–vis absorption spectra of *p*-NP solution recorded at different time intervals after the addition of (a) 1Ag@Py-PZ, (b) 3Ag@Py-PZ, (c) 1Ag@TPE-PZ, and (d) 3Ag@TPE-PZ CMPs. (e) Time-dependent changes in the relative absorbance (A/A_0) during the reduction of 4-NP. (f) Pseudo-first-order kinetic plots for the reduction of *p*-NP catalyzed by 1Ag@Py-PZ, 3Ag@Py-PZ, 1Ag@TPE-PZ, and 3Ag@TPE-PZ CMPs.

faster catalytic conversion than 3Ag@TPE-PZ CMP. This superior activity is primarily attributed to the more planar and structurally rigid framework of the Py-PZ CMP, which promotes improved dispersion and surface accessibility of Ag nanoparticles. In addition, the extended conjugation and reduced steric hindrance of the pyrene-based backbone enable more efficient electron transport along the polymer network, accelerating interfacial electron transfer to the Ag active sites. These results confirm that both silver content and polymer architecture critically govern the catalytic activity of Ag@PZ CMPs, with higher Ag loading and the pyrene-based framework providing the most efficient reduction of *p*-NP. To further assess catalytic efficiency, the reduction of *p*-NP was tracked by plotting the normalized absorbance ratio (A/A_0) at 400 nm as a function of time for all four Ag@PZ CMP catalysts [Fig. 5 (e)]. In each case, A/A_0 decreases steadily over time, reflecting the progressive conversion of *p*-NP to *p*-AP. A clear kinetic trend is observed: catalysts with higher Ag loading induce a more rapid decline in A/A_0, and within each loading level, the Py-PZ-based CMPs exhibit faster reaction rates than the TPE-PZ-based analogues. Notably, 3Ag@Py-PZ CMP displays the steepest decay curve, followed by 1Ag@Py-PZ CMP, 3Ag@TPE-PZ CMP, and finally 1Ag@TPE-PZ CMP. This ranking demonstrates the synergistic influence of both silver quantity and the CMP framework on catalytic performance. The competitive decline of A/A_0 highlights that catalytic reduction is governed by the dispersion, accessibility, and interfacial exposure of Ag nanoparticles, as well as the intrinsic electron-conducting properties of the polymer network.

Compared with the bulkier and less rigid TPE-PZ CMP, the planar Py-PZ CMP offers more exposed active interfaces and shorter electron-migration pathways, resulting in faster heterogeneous electron transfer and improved catalytic turnover. The kinetic trends derived from A/A_0 monitoring closely match the observations from time-dependent UV–Vis spectroscopy, collectively validating the beneficial role of enhanced Ag loading and pyrene-induced structural planarity in promoting heterogeneous catalytic activity. Finally, the catalytic reduction rates of the four Ag@PZ-CMP nanocomposites were quantitatively analyzed using a pseudo-first-order kinetic model. The apparent rate constants (k_{app}) were extracted from the linear plots of $\ln(A/A_0)$ versus time [Fig. 5(f)], which further reveal the strong dependence of catalytic efficiency on both Ag content and PZ-CMP backbone structure. For the Ag-anchored Py-PZ CMP catalysts, 3Ag@Py-PZ CMP exhibits the highest catalytic activity, delivering the largest apparent rate constant ($k_{app} = 29 \times 10^{-3}\ s^{-1}$) and the fastest normalized reduction rate ($k_{nor} = 58$ mg s^{-1}), followed by 1Ag@Py-PZ CMP ($k_{app} = 15 \times 10^{-3}\ s^{-1}$, $k_{nor} = 39.4$ mg s^{-1}). This trend confirms that increasing Ag loading increases the number of accessible active sites, which in turn accelerates the reduction reaction. In contrast, the TPE-PZ CMP series shows overall lower catalytic performance. Within this framework, 3Ag@TPE-PZ CMP ($k_{app} = 18 \times 10^{-3}\ s^{-1}$, $k_{nor} = 36$ mg s^{-1}) outperforms 1Ag@TPE-PZ CMP ($k_{app} = 2 \times 10^{-3}\ s^{-1}$, $k_{nor} = 4$ mg s^{-1}). The reduced activity of the TPE-based catalysts is attributed to their bulkier and less planar polymer structure, which restricts Ag nanoparticle dispersion and limits active-site accessibility. Despite this, the observed rates remain highly competitive compared with reported Ag-anchored nanocomposites [Table S2] [22,64–72]. A direct comparison between the two PZ-CMP frameworks at identical Ag loading further demonstrates that Py-PZ CMP consistently exhibits faster reaction kinetics than TPE-PZ CMP, highlighting the importance of polymer architecture. The rigid, planar pyrene-based backbone enhances electron transfer and enables more effective exposure of catalytic sites, leading to superior catalytic efficiency. Together, these results quantitatively validate earlier UV–Vis observations and confirm that both Ag content and polymer framework structure are critical factors governing catalytic performance in Ag@PZ- CMP nanocomposites. The reduction of nitroaromatic compounds over the Ag/CMP catalysts in the presence of $NaBH_4$ is proposed to follow the well-established stepwise hydrogenation pathway typical for noble-metal nanoparticle systems. In this mechanism, Ag nanoparticles act as electron-transfer mediators, adsorbing both BH_4^- and the nitro substrate and facilitating surface hydride transfer. The nitro group is sequentially reduced through nitroso (–NO) and hydroxylamine (–NHOH) intermediates before finally forming the corresponding amine ($–NH_2$). Although these intermediates are generally short-lived and difficult to directly detect under the rapid reaction conditions employed here, this pathway is widely reported in metal nanoparticle-catalyzed reductions and is consistent with the efficient catalytic performance observed in our system (Scheme 1).

The catalytic efficiency of the Ag@Py-PZ CMP nanocomposites was further evaluated using turnover number (TON) and turnover frequency (TOF) as performance metrics [Fig. 6]. TON is defined as the number of *p*-nitrophenol molecules converted per mole of Ag catalyst, whereas TOF refers to the number of substrate molecules converted per mole of catalyst per unit time, offering key insight into the intrinsic activity of the catalysts. For 1Ag@Py-PZ CMP, the TON values [Fig. 6(a)] increase consistently over time, reaching approximately 50.9 after 4 min, demonstrating the efficient utilization of accessible silver active sites. In contrast, 3Ag@Py-PZ CMP exhibits lower TON values (≈31.3 at 4 min) despite its higher silver content. This trend arises because TON is normalized to the number of silver moles, meaning that increasing the Ag loading results in a lower TON per active site, even when the overall conversion rate is higher. The TOF values exhibit a similar trend.

For 1Ag@Py-PZ CMP, the TOF begins at a high value (≈21.9 min^{-1}) and gradually declines to ≈12.7 h^{-1} at 4 min, which is consistent with progressive substrate depletion and the corresponding reduction in reaction rate. Likewise, 3Ag@Py-PZ CMP shows lower TOF values overall (≈11.2 h^{-1} initially, decreasing to ≈7.8 h^{-1}), again due to normalization per mole of Ag. The lower TON/TOF for 3Ag@Py-PZ CMP compared to 1Ag@Py-PZ CMP, despite its higher absolute conversion rate, underscores that these metrics normalize activity to the total moles of Ag. This suggests that not all incorporated Ag atoms are equally surface-accessible or catalytically active under the given conditions. The catalytic performance of 1Ag@TPE-PZ CMP and 3Ag@TPE-PZ CMP was further assessed through TON and TOF analyses for the reduction of nitro compounds [Fig. 6(b)]. For both catalysts, the TON values increase steadily with reaction time, confirming sustained catalytic turnover and

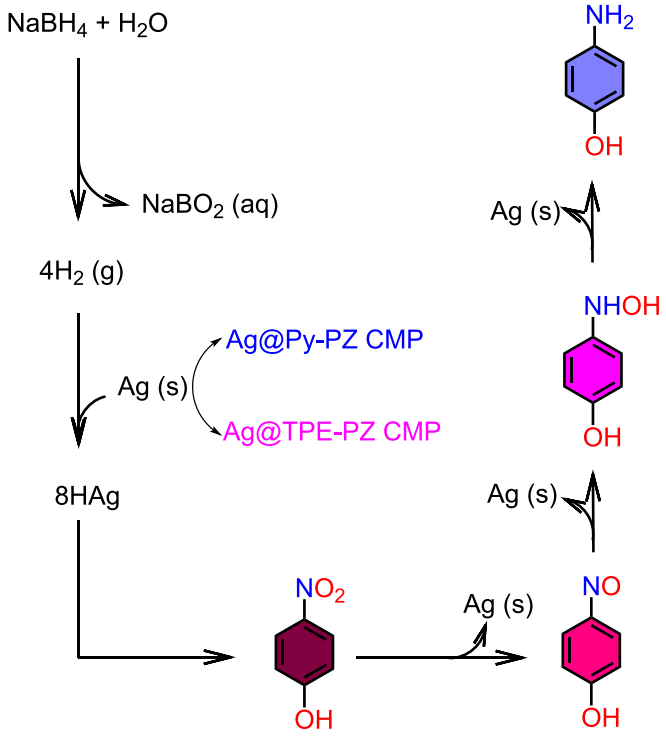

Scheme 1. The proposed conversion mechanism of *p*-NP into *p*-AP.

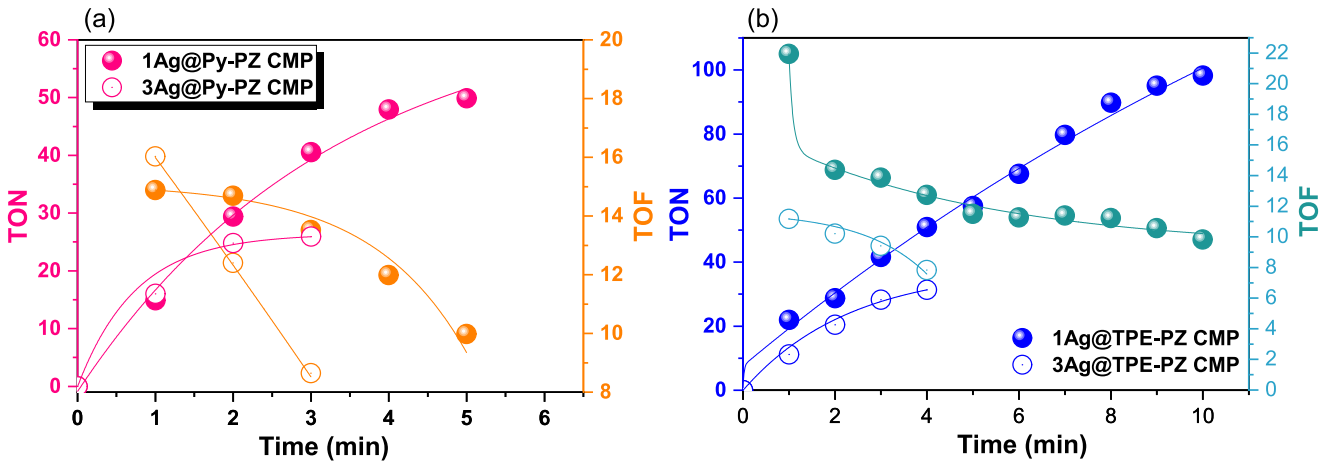

Fig. 6. TON and TOF of the catalytic system using (a) 1Ag@Py-PZ and 3Ag@Py-PZ CMPs, and (b) 1Ag@TPE-PZ and 3Ag@TPE-PZ CMPs.

the effective use of Ag active sites. At each reaction stage, 3Ag@TPE-PZ CMP displays higher TON values than 1Ag@TPE-PZ CMP, which can be attributed to its greater Ag loading and the larger number of accessible catalytic sites. In contrast, the TOF values decrease gradually over time for both catalysts, an expected behavior in heterogeneous catalytic systems, primarily driven by substrate consumption and the partial occupation of active sites by reaction intermediates or products. Notably, 3Ag@TPE-PZ CMP retains higher TOF values throughout the reaction, indicating accelerated reaction kinetics and superior intrinsic catalytic activity compared to 1Ag@TPE-PZ CMP. The TON and TOF results were benchmarked against previously reported catalytic moieties for *p*-nitrophenol reduction (Table S3). To evaluate the intrinsic catalytic contribution of the polymer frameworks, pristine Py-PZ CMP and TPE-PZ CMP were tested under identical reaction conditions for the reduction of *p*-NP in the presence of $NaBH_4$ [Fig. S6]. The UV–Vis spectra show only a slight decrease in absorbance at 400 nm, changing from 4.03 to 3.01 a.u. for Py-PZ CMP and from 4.03 to 3.44 a.u. for TPE-PZ CMP. This minimal change indicates that the undecorated CMPs exhibit weak adsorption toward *p*-NP and contribute negligibly to its catalytic reduction. These control experiments confirm that the catalytic activity observed in the Ag-decorated PZ-CMPs originates predominantly from the silver nanoparticles, rather than from the polymer matrix itself, further confirming that any trace Pd does not contribute to the observed catalytic performance. The minor decline in absorbance is likely attributable to *p*-NP adsorption onto the CMP surfaces, which aligns with the hierarchical porosity and accessible surface sites inherent

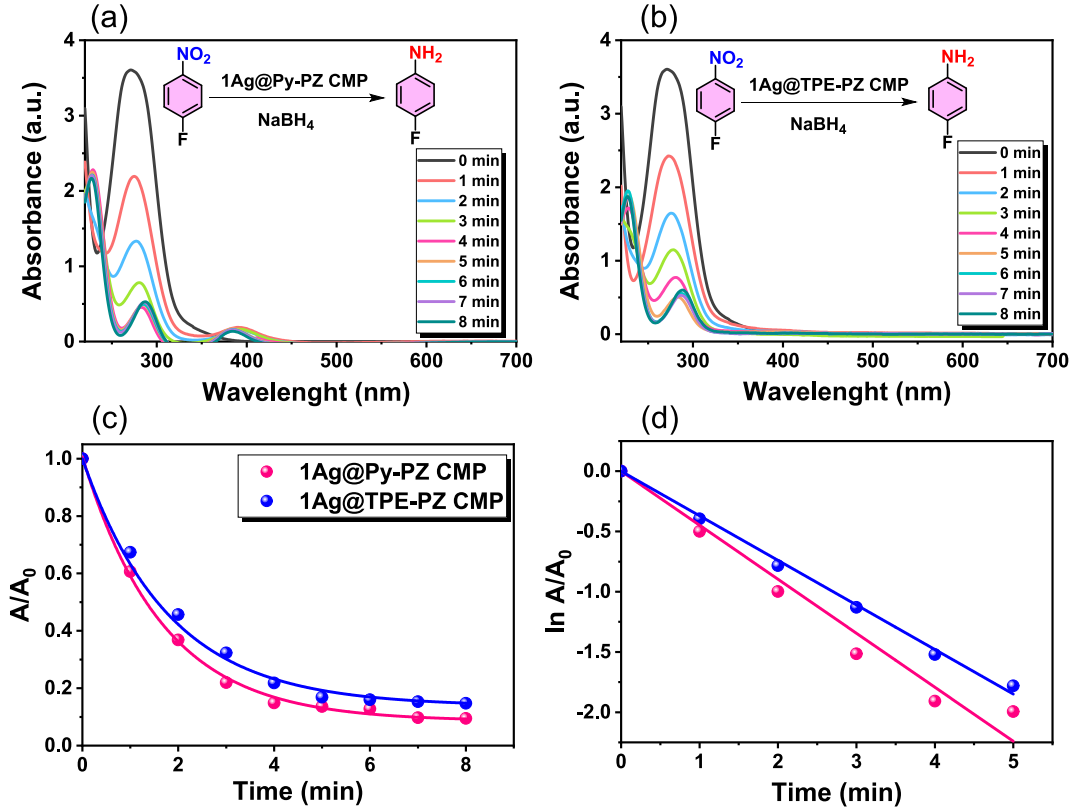

Fig. 7. UV–vis spectra of *p*-FNB solution recorded during reduction in the presence of 1Ag@Py-PZ (a) and 1Ag@TPE-PZ (b) CMPs. (c) Time-dependent changes in relative absorbance and (d) pseudo-first-order kinetic plotsfor *p*-FNB reduction catalyzed by 1Ag@Py-PZ and 1Ag@TPE-PZ CMPs.

to these CMP frameworks. The catalytic performance of 1Ag@Py-PZ CMP and 1Ag@TPE-PZ CMP was further assessed using *p*-FNB as the substrate in a $NaBH_4$ reduction system [Fig. 7(a) and (b)]. In this case, the initial UV–Vis spectra display a strong absorption band at 270 nm, characteristic of the nitro compound, which diminishes rapidly after catalyst addition. The decrease is substantially more pronounced for 1Ag@Py-PZ CMP, indicating a faster conversion rate relative to 1Ag@TPE-PZ CMP and suggesting superior catalytic efficiency and reaction kinetics.

Time-dependent monitoring of the normalized absorbance (A/A_0) further supports this trend, showing a significantly faster decline for the 1Ag@TPE-PZ CMP catalyst [Fig. 7(c)]. Pseudo-first-order kinetic analysis yields apparent rate constants (k_{app}) of 0.448 min^{-1} for 1Ag@Py-PZ CMP and 0.369 min^{-1} for 1Ag@TPE-PZ CMP, quantitatively confirming the superior catalytic efficiency of the Py-PZ framework [Fig. 7(d)]. These results suggest that the planar and rigid pyrene-containing polymer backbone facilitates more uniform Ag nanoparticle dispersion and provides a higher degree of active-site accessibility, which collectively promote improved electron transfer and stronger substrate-catalyst interactions. In contrast, the sterically bulkier TPE-PZ CMP leads to slightly reduced catalytic activity, likely due to less efficient nanoparticle distribution and comparatively limited substrate accessibility. To further evaluate the substrate scope and functional group tolerance of the catalysts, additional nitroaromatic compounds bearing different substituents were investigated. Besides *p*-NP and *p*-FNB, p-nitroaniline (*p*-NA) (Fig. S7) and 1-chloro-4-nitrobenzene (Fig. S8) were also tested under identical reaction conditions. Both substrates were efficiently reduced to their corresponding amine products with high conversion, demonstrating that the Ag@PZ CMP catalysts exhibit broad applicability toward structurally diverse nitroarenes. These results confirm the general catalytic versatility and robustness of the developed nanocomposites. The stability and reusability of 1Ag@Py-PZ CMP and 1Ag@TPE-PZ CMP were assessed over five consecutive catalytic cycles using *p*-NP reduction as the model reaction. Both catalysts maintained high conversion throughout the cycling tests. The pyrene-based catalyst (1Ag@Py-PZ CMP) exhibited conversion efficiencies of 100%, 97%, 93%, 91%, and 90%, while 1Ag@TPE-PZ CMP achieved 100%, 99%, 96%, 93%, and 91% [Fig. S9(a)]. The gradual yet limited decline in activity indicates that both catalysts possess excellent operational stability and recyclability. FTIR spectra of Ag@Py-PZ and Ag@TPE-PZ CMPs collected after the fifth cycle show no notable changes relative to the pristine materials, confirming that the chemical structures of the CMP frameworks remain intact after repeated catalytic use [Fig. S9(b) and (c)]. Moreover, TEM analysis on the recycled catalysts reveals that the Ag nanoparticles remain uniformly dispersed and that the overall morphology of the CMP framework shows almost no obvious change, with no significant nanoparticle aggregation or structural collapse observed (Fig. S10). Although gradual adsorption of reaction intermediates or by-products could potentially block some active sites during very long-term operation, such effects were not evident within the investigated cycles. Collectively, these results demonstrate that both Ag-decorated PZ-CMPs are highly robust heterogeneous catalysts, offering strong durability and structural resilience, which underscore their potential for practical and long-term catalytic applications.

4. Conclusions

Two Py-PZ CMP and TPE-PZ CMP were synthesized via Sonogashira-Hagihara coupling and systematically characterized in terms of porosity, thermal stability, and morphology. Both Py-PZ CMP and TPE-PZ CMP incorporate amino functional groups capable of inducing *in-situ* reduction of Ag^+, enabling the formation of Ag-decorated hybrids (Ag@Py-PZ CMP and Ag@TPE-PZ CMP) with uniformly dispersed Ag nanoparticles. The catalytic performance of the Ag@PZ-CMPs was evaluated for the $NaBH_4$-mediated reduction of *p*-NP and *p*-FNB, confirming their function as efficient heterogeneous catalysts. The Py-PZ-based CMP catalyst exhibited consistently higher catalytic activity than the TPE-PZ CMP, likely due to its planar, rigid backbone, which promotes improved Ag nanoparticle dispersion, greater active-site accessibility, and more effective electron transfer. Increasing Ag content further enhanced reaction kinetics, demonstrating a clear loading-dependent catalytic trend. Pseudo-first-order kinetic fitting, together with TON and TOF analyses, quantitatively confirmed high catalytic efficiency, while TON/TOF trends correlated positively with Ag incorporation. Control experiments with pristine CMPs showed negligible catalytic contribution beyond weak substrate adsorption, verifying that Ag nanoparticles are the primary active catalytic component. Notably, both catalysts retained high activity over five reuse cycles, with no significant structural degradation observed. Overall, this study presents a straightforward and effective strategy for constructing durable, high-performance, and recyclable Ag-decorated PZ-based CMP catalysts for nitro-compound reduction reactions, offering strong potential for practical catalytic applications.

CRediT authorship contribution statement

Aya Osama Mousa: Writing – original draft, Formal analysis, Data curation. **Mohamed Gamal Mohamed:** Writing – review & editing, Writing – original draft, Supervision, Methodology, Investigation, Formal analysis, Data curation, Conceptualization. **Mohammed G. Kotp:** Formal analysis, Data curation. **Shiao-Wei Kuo:** Supervision, Resources, Funding acquisition.

Declaration of competing interest

The authors declare that they have no known competing financial interests or personal relationships that could have appeared to influence the work reported in this paper.

Acknowledgments

This study was supported financially by the National Science and Technology Council, Taiwan, under contracts NSTC 114-2223-E-110-001- and 113-2221-E-110-012-MY3. The authors thank the staff at National Sun Yat-sen University for their assistance with the TEM (ID: EM022600) experiments.

Appendix A. Supplementary data

Supplementary data to this article can be found online at https://doi.org/10.1016/j.eurpolymj.2026.114599.

Data availability

Data will be made available on request.

References

[1] X. Luo, A. Zhang, L. Wu, Y. Fu, Rapid biosynthesis of highly active gold nanoparticles for colorimetric detection of p-phenylenediamine and p-nitrophenol reduction in wastewater, J. Environ. Chem. Eng. 12 (2024) 112036, https://doi.org/10.1016/j.jece.2024.112036.
[2] S. Thomas, D.O.B. Apriandanu, A. Umar, R. Bakri, M. Khalil, $NiFe_2O_4$/Multi-walled carbon nanotubes composite for catalytic reduction of p-Nitrophenol, Surf. Interfaces 64 (2025) 106459, https://doi.org/10.1016/j.surfin.2025.106459.
[3] H. Wang, L. Chang, X. Duan, X. Ren, Sb-doped SnO_2 nanoflowers/Ti/TiO_2-nanotubes bifacial electrode for enhanced photoelectrocatalytic degradation of p-nitrophenol, Environ. Res. 291 (2025) 123521, https://doi.org/10.1016/j.envres.2025.123521.
[4] H. Wang, X. Sui, S. Geng, X. Zhao, X. Duan, A novel Sb-doped SnO_2 nanoflower anode for the efficient degradation of p-nitrophenol, J. Water Process Eng. 77 (2025) 108334, https://doi.org/10.1016/j.jwpe.2025.108334.
[5] M. Wang, Q. Liu, L. Li, D. Wang, Y. Zou, J. Hu, Y. Xiao, Y. Lan, Y. Yang, X. Guo, Construction of carbazole-conjugated dual-emission fluorescent covalent organic framework for distinguishing p-nitroaniline/p-nitrophenol and adsorbing

nitroanilines/nitrophenols, J. Hazard. Mater. 483 (2025) 136631, https://doi.org/10.1016/j.jhazmat.2024.136631.
[6] A. Feng, C. Lin, H. Zhou, W. Jin, Y. Hu, D. Li, Q. Li, Catalytic transformation of 4-nitrophenol into 4-aminophenol over ZnO nanowire array-decorated cu nanoparticles, Green, Chem. Eng. 5 (2024) 205–212, https://doi.org/10.1016/j.gce.2023.03.003.
[7] L. Yao, Y. Dai, Y. Ding, H. Jiang, One-step synthesis of N-doped spider-web-like hyper-cross-linked polymers by a knitting strategy for efficient removal of phenolic pollutants, Sep. Purif. Technol. 361 (2025) 131445, https://doi.org/10.1016/j.seppur.2025.131445.
[8] X. Cao, X. Lei, R. Wang, H. Zhao, S. Xiong, H. Zhai, D. Zhang, H. Fan, Q. Liu, Magnetic amine–modified pitch–based hypercrosslinked polymers for high–efficiency adsorption of phenolic pollutants, Polymer 339 (2025) 129138, https://doi.org/10.1016/j.polymer.2025.129138.
[9] Y. Zang, Y. Liu, R. Hou, Z. He, B. Wei, J. Wang, J. Liu, L. Xu, R. Xie, W. Zhang, Silver nanoparticle-loaded conjugated microporous polymers: a highly efficient photocatalyst for methylene blue degradation, Macromol. Rapid Commun. 46 (2025) e00628, https://doi.org/10.1002/marc.202500628.
[10] P. Ran, F. Wei, B. Xiang, A. Qiu, B. Tian, X. Xu, L. Dai, H. Zhang, F. Wang, Y. Sun, Efficient, versatile, and durable electrocatalytic nitroaromatic-to-arylamine reduction via heteroatom-site hydrogen-atom transfer, J. Am. Chem. Soc. 147 (2025) 37414–37427, https://doi.org/10.1021/jacs.5c11419.
[11] S.M. Shaban, B.-S. Moon, D.-H. Kim, Selective and sensitive colorimetric detection of p-aminophenol in human urine and paracetamol drugs based on seed-mediated growth of silver nanoparticles, Environ. Technol. Innov. 22 (2021) 101517, https://doi.org/10.1016/j.eti.2021.101517.
[12] Y. Zhang, Q. Xie, Z. Xia, G. Gui, P. Zhang, L. Meng, L. Pan, Amino β-cyclodextrin-functionalized GS/MWCNTs for simultaneous electrochemical determination of p-aminophenol and acetaminophen, Int. J. Electrochem. Sci. 17 (2022) 221172, https://doi.org/10.20964/2022.11.76.
[13] M.G. Kotp, M.G. Mohamed, A.O. Mousa, S.-W. Kuo, Rational design and molecular engineering of ultrastable porous fluorescent guanidine functionalized polybenzoxazine, Eur. Polym. J. 227 (2025) 113786, https://doi.org/10.1016/j.eurpolymj.2025.113786.
[14] Z. Deliballi, B. Kiskan, Y. Yagci, Main-chain benzoxazine precursor block copolymers, Polym. Chem. 9 (2018) 178–183, https://doi.org/10.1039/C7PY01873H.
[15] A. Goel, M. Rani, A novel method for the remediation of o-and p-aminophenol from industrial wastewater by hexacyanoferrate (III) ions using Ir-complex catalyst, Environ. Qual. Manag. 34 (2024) e22205, https://doi.org/10.1002/tqem.22205.
[16] Y. Zheng, S. Lei, W. Guo, W. Xiang, Y. Chen, Y. Zhang, Fabrication of core-shell MIL-125-NH_2@ ZIF-67/SiO_2 composites with enhanced catalytic activity for nitroaromatic reduction, J. Environ. Chem. Eng. 13 (2025) 118393, https://doi.org/10.1016/j.jece.2025.118393.
[17] T.H. Habeeb, U. Farooq, Advanced strategies for plastic upcycling: unlocking sustainable waste valorization pathways for a green and sustainable environment, Catal Sci. Technol. 15 (2025) 5602–5634, https://doi.org/10.1039/D5CY00477B.
[18] L. Bai, Z. Gong, Y. Yu, J. Wang, Z. Chen, J. Wang, S. Li, Dendritic Cu–Co_3O_4 with Elevated oxygen vacancies for the degradation of organic pollutants, ACS Appl. Nano Mater. 8 (2025) 23288–23299, https://doi.org/10.1021/acsanm.5c04727.
[19] D.S. Deshmukh, S. Singh, K.C. Badgujar, V.T. Humne, G.V. Korpe, B.M. Bhanage, Green innovations in C–H bond functionalisation: exploring homogeneous recyclable catalytic systems, Green Chem. 27 (2025) 5667–5708, https://doi.org/10.1039/D5GC00278H.
[20] S.I. Sanakal, A. Das, A. Babu, P. Kar, V. Nutalapati, K. Datta, S. Banerjee, S. Maji, Alginate-aminoclay/CuO nanocomposite beads: a sustainable and green approach for catalytic reduction of toxic nitroaromatic compounds, J. Environ. Chem. Eng. 13 (2025) 115398, https://doi.org/10.1016/j.jece.2025.115398.
[21] A.O.C. Iroegbu, M.L. Teffo, E.R. Sadiku, R. Meijboom, S.P. Hlangothi, Advancing wastewater treatment with green and scalable metal–organic frameworks: from synthetic strategies to real-world deployment, npj Clean Water 8 (2025) 85, https://doi.org/10.1038/s41545-025-00514-x.
[22] H. Cao, H.-B. Huang, Z. Chen, B. Karadeniz, J. Lü, R. Cao, Ultrafine silver nanoparticles supported on a conjugated microporous polymer as high-performance nanocatalysts for Nitrophenol Reduction, ACS Appl. Mater. Interfaces 9 (2017) 5231–5236, https://doi.org/10.1021/acsami.6b13186.
[23] S. Fajal, S. Dutta, S.K. Ghosh, Porous organic polymers (POPs) for environmental remediation, Mater. Horiz. 10 (2023) 4083–4138, https://doi.org/10.1039/D3MH00672G.
[24] S. Ge, K. Wei, W. Peng, R. Huang, E. Akinlabi, H. Xia, M.W. Shahzad, X. Zhang, B. B. Xu, J. Jiang, A comprehensive review of covalent organic frameworks (COFs) and their derivatives in environmental pollution control, Chem. Soc. Rev. 53 (2024) 11259–11302, https://doi.org/10.1039/D4CS00521J.
[25] Q. Sun, B. Aguila, Y. Song, S. Ma, Tailored porous organic polymers for task-specific water purification, Acc. Chem. Res. 53 (2020) 812–821, https://doi.org/10.1021/acs.accounts.0c00007.
[26] C.G. Bezzu, M. Carta, A. Tonkins, J.C. Jansen, P. Bernardo, F. Bazzarelli, N. B. McKeown, A Spirobifluorene-based polymer of intrinsic microporosity with improved performance for gas separation, Adv. Mater. 24 (2012) 5930–5933, https://doi.org/10.1002/adma.201202393.
[27] M.G. Mohamed, A.F.M. EL-Mahdy, M.G. Kotp, S.-W. Kuo, Advances in porous organic polymers: syntheses, structures, and diverse applications, Mater. Adv. 3 (2022) 707-733. DOI: 10.1039/D1MA00771H.
[28] Y. Zhang, S.N. Riduan, Functional porous organic polymers for heterogeneous catalysis, Chem. Soc. Rev. 41 (2012) 2083–2094, https://doi.org/10.1039/C1CS15227K.
[29] S.L. Cai, Y.B. Zhang, A.B. Pun, B. He, J. Yang, F.M. Toma, I.D. Sharp, O.M. Yaghi, J. Fan, S.R. Zheng, W.G. Zhang, Y. Liu, Tunable electrical conductivity in oriented thin films of tetrathiafulvalene-based covalent organic framework, Chem. Sci. 5 (2014) 4693–4700, https://doi.org/10.1039/C4SC02593H.
[30] S.Y. Ding, J. Gao, Q. Wang, Y. Zhang, W.G. Song, C.Y. Su, W. Wang, Construction of covalent organic framework for catalysis: Pd/COF-LZU1 in Suzuki−Miyaura coupling reaction, J. Am. Chem. Soc. 133 (2011) 19816–19822, https://doi.org/10.1021/ja206846p.
[31] M.G. Kotp, M.G. Mohamed, S.-W. Kuo, Conjugated microporous polymer electrodes for supercapacitors: recent progress, key challenges, and future directions, Chem. Sci. 16 (2025) 20718–20754, https://doi.org/10.1039/D5SC05384F.
[32] A.O. Mousa, M.G. Mohamed, Z.-I. Lin, C.-H. Chuang, C.-K. Chen, S.-W. Kuo, Construction of cationic conjugated microporous polymers containing pyrene units through post-cationic modification for enhanced antibacterial performance, J. Taiwan Inst. Chem. Eng. 157 (2024) 105448, https://doi.org/10.1016/j.jtice.2024.105448.
[33] Y. Liao, J. Zeng, S. Kang, Q. Wu, H. Cui, W. Zhang, B. Yi, C. Liu, H. Yang, Strengthening hydrogen bonds of clay/conjugated microporous polymer composites for advancing visible-light-driven antibiotic removal, Sep. Purif. Technol. 387 (2026) 136589, https://doi.org/10.1016/j.seppur.2025.136589.
[34] W. Zhang, X. Luo, L. Liu, M. Lei, Q. Wan, B. Yi, F. Yu, H. Yang, Engineering exciton dissociation and intermolecular charge transfer to boost superoxide radical in conjugated microporous polymers for simultaneous elimination of coexisting contaminants, Chem. Eng. J. 499 (2024) 156552, https://doi.org/10.1016/j.cej.2024.156552.
[35] Y. Wang, Y. Yang, Q. Deng, W. Chen, Y. Zhang, Y. Zhou, Z. Zou, Recent progress of amorphous porous organic polymers as heterogeneous photocatalysts for organic synthesis, Adv. Funct. Mater. 33 (2023) 2307179, https://doi.org/10.1002/adfm.202307179.
[36] A.O. Mousa, M.G. Mohamed, Z.-I. Lin, C.-H. Chuang, C.-K. Chen, S.-W. Kuo, Conjugated microporous polymers as a novel generation of drug carriers: a systemic study toward efficient carriers of tetracycline antibiotic, Eur. Polym. J. 196 (2023) 112254, https://doi.org/10.1016/j.eurpolymj.2023.112254.
[37] M.G. Mohamed, W.C. Huang, M. Ejaz, Y.C. Kao, Y.M. Lo, A.A.K. Mohammed, Y. L. Kuan, S.W. Kuo, Ferrocene-linked triazine-based porous organic polymers as multifunctional platforms for CO_2 recognition, separation and utilization, J. CO_2 Util. 105 (2026) 103356, https://doi.org/10.1016/j.jcou.2026.103356.
[38] A.O. Mousa, Z.-I. Lin, C.-H. Chuang, C.-K. Chen, S.-W. Kuo, M.G. Mohamed, Rational design of bifunctional microporous organic polymers containing anthracene and triphenylamine units for energy storage and biological applications, Int. J. Mol. Sci. 24 (2023) 8966, https://doi.org/10.3390/ijms24108966.
[39] M.G. Mohamed, C.-C. Chen, M. Ibrahim, A.O. Mousa, M.H. Elsayed, Y. Ye, S.-W. Kuo, Tetraphenylanthraquinone and dihydroxybenzene-tethered conjugated microporous polymer for enhanced CO_2 uptake and supercapacitive energy storage, JACS Au 4 (2024) 3593–3605, https://doi.org/10.1021/jacsau.4c00537.
[40] M.G. Mohamed, M.G. Kotp, A.O. Mousa, Y.-S. Li, S.-W. Kuo, Construction of Fe-and N-Doped microporous carbon from ferrocene-based conjugated microporous polymers for supercapacitive energy storage, ACS Appl. Energy Mater. 4 (2025) 2389–2402, https://doi.org/10.1021/acsaem.4c02968.
[41] X. Deng, R. Xiang, M. Liu, B. Yi, W. Zhang, C. Liu, H. Yang, Molecular oxygen activation mediated by exciton effects in CMPs@Sepiolite for photocatalytic elimination of emerging contaminants, Chem. Eng. J. 527 (2026) 171570, https://doi.org/10.1016/j.cej.2025.171570.
[42] W. Liu, Z. Zhu, Y. Zong, J. Wang, C. Guo, M. Li, R. Jiao, F. Wang, H. Sun, A. Li, Efficient adsorption of lead ions by sulfur-rich conjugated microporous polymers aerogels with high selectivity, J. Colloid Interface Sci. 697 (2025) 137956, https://doi.org/10.1016/j.jcis.2025.137956.
[43] P. Wang, F. Ma, N. Huang, G. Liang, Y. Zheng, L.L. Tan, Y. Yan, M. Liu, L. Ye, Triazine engineering in conjugated microporous polymers for hydrogen peroxide photosynthesis, Adv. Funct. Mater. 36 (2025) 2507907, https://doi.org/10.1002/adfm.202507907.
[44] H. Ren, X. Zhao, Z. Lang, H. Tan, Y. Wang, Y. Li, β-Ketoenamine linkage-engineered donor–acceptor covalent heptazine polymers for efficient visible-light-driven overall water splitting, Chem. Eng. J. 526 (2025) 170975, https://doi.org/10.1016/j.cej.2025.170975.
[45] K.A. Sanoja-López, R. Luque, Porous materials for the heterogeneously catalyzed synthesis of high value-added products: latest trends and future prospects, Chem. Asian J. 20 (2025) e202401238, https://doi.org/10.1002/asia.202401238.
[46] W. Song, Y. Wen, Y. Cho, X. Zhang, D. Kang, E. Shin, D.G. Yu, G. Li, Y. Liao, I. D. Kim, Advances and prospects in multifunctional composite fibrous materials utilizing porous organic polymers, Adv. Mater. 38 (2025) e13138, https://doi.org/10.1002/adma.202513138.
[47] M. Qi, X. Wang, J. Chen, Y. Liu, Y. Liu, J. Jia, L. Li, T. Yue, L. Gao, B. Yan, Transformation, absorption and toxicological mechanisms of silver nanoparticles in the gastrointestinal tract following oral exposure, ACS Nano 17 (2023) 8851–8865, https://doi.org/10.1021/acsnano.3c00024.
[48] X. Cheng, X. Pei, W. Xie, J. Chen, Y. Li, J. Wang, H. Gao, Q. Wan, pH-triggered size-tunable silver nanoparticles: targeted aggregation for effective bacterial infection therapy, Small 18 (2022) 2200915, https://doi.org/10.1002/smll.202200915.
[49] K. Subodh, D.T. Prakash, Masram, silver nanoparticles immobilized covalent organic microspheres for hydrogenation of nitroaromatics with intriguing catalytic activity, ACS Appl. Polym. Mater. 3 (2020) 310–318, https://doi.org/10.1021/acsapm.0c01111.

[50] J. Lee, J.G. Kim, J.Y. Chang, Fabrication of a conjugated microporous polymer membrane and its application for membrane catalysis, Sci. Rep. 7 (2017) 13568, https://doi.org/10.1038/s41598-017-13827-w.
[51] X. He, M. Chen, J. Lv, H. Xiao, H. Wu, R. Zhou, J. Hu, K. Zeng, G. Yang, A theoretical investigation on the chemical environment of pyrazine-2,3-dicarbonitrile and phthalonitrile: Density functional theory (DFT) calculation and experimental verification, J. Mol. Struct. 1292 (2023) 136117, https://doi.org/10.1016/j.molstruc.2023.136117.
[52] C.L. Anderson, T. Zhang, M. Qi, Z. Chen, C. Yang, S.J. Teat, N.S. Settineri, E. A. Dailing, A. Garzón-Ruiz, A. Navarro, Exceptional electron-rich heteroaromatic pentacycle for ultralow band gap conjugated polymers and photothermal therapy, J. Am. Chem. Soc. 145 (2023) 5474–5485, https://doi.org/10.1021/jacs.3c00036.
[53] R.S. Rao, J.V.S. Krishna, U.R. Gandra, I.F. Perepichka, J. Shaya, Pyrazine-based sensitizers for dye-sensitized solar cells, Mater. Chem. Front. 9 (2025) 2120–2160, https://doi.org/10.1039/D4QM01100G.
[54] Y. Bai, J. Deng, W. Xie, J. Xiao, J. Zhang, Y. Wang, X. Guo, H. Wang, Pyrazine as a more efficient luminophore than benzene for producing red-shifted and enhanced photoluminescence, J. Phys. Chem. A 127 (2023) 9273–9282, https://doi.org/10.1021/acs.jpca.3c05506.
[55] P. Zhang, Y. Chen, Y. Liu, J. Wei, Z. Wu, B. Yang, G. Ding, S. Wen, T. Dai, Z. You, Unlocking multielectron transfer in a quinone–pyrazine conjoined redox core for capacity-doubled and ultrastable aqueous organic redox flow batteries, J. Am. Chem, Soc. J. Am. Chem. Soc. 147 (2025) 46582–46593, https://doi.org/10.1021/jacs.5c17809.
[56] J. Xu, Y. Bi, H. Zhao, L. Shi, N. Zhang, X. Xin, In situ synthesis of well-dispersed silver nanoparticles from silver nanoclusters hydrogel for catalytic reduction of 4-Nitrophenol, Appl. Surf. Sci. 683 (2025) 161759, https://doi.org/10.1016/j.apsusc.2024.161759.
[57] F. Zhang, Q. Yao, Y. Niu, X. Chen, H. Zhou, L. Bai, Z. Kong, Y. Li, H. Cheng, In situ fabrication of silver nanoparticle-decorated polymeric vesicles for antibacterial applications, ChemistryOpen 13 (2024) e202300223, https://doi.org/10.1002/open.202300223.
[58] A.O. Mousa, Z.-I. Lin, S.V. Chaganti, C.-H. Chuang, C.-K. Chen, S.-W. Kuo, M. G. Mohamed, Bifunctional imidazolium linked tetraphenylethene based conjugated microporous polymers for dynamic antibacterial properties and supercapacitor electrodes, Polym. Chem. 15 (2024) 397–411, https://doi.org/10.1039/D3PY01303K.
[59] M.G. Kotp, M.G. Mohamed, P.-T. Wang, A.E. Hassan, A.M. Elewa, S.-W. Kuo, Unlocking the potential of *N*,*N*,*N*′,*N*′-tetraphenylbenzidine based on conjugated microporous polymers for rhodamine B adsorption: a synergistic experimental and density functional theory perspective, ACS Polym. Au 4 (2025) 379–393, https://doi.org/10.1021/acspolymersau.5c00025.
[60] A.O. Mousa, S.U. Sharma, S.V. Chaganti, T.H. Mansoure, P.N. Singh, M. Ejaz, C.-H. Chuang, J.-T. Lee, S.-W. Kuo, M.G. Mohamed, Designing strategically functionalized conjugated microporous polymers with pyrene and perylenetetracarboxylic dianhydride moieties with single-walled carbon nanotubes to enhance supercapacitive energy storage efficiency, J. Power Sources 608 (2024) 234624, https://doi.org/10.1016/j.jpowsour.2024.234624.
[61] N. Nikolić, J. Spasojević, A. Radosavljević, M. Milošević, T. Barudžija, L. Rakočević, Z. Kačarević-Popović, Influence of poly (vinyl alcohol)/poly (N-vinyl-2-pyrrolidone) polymer matrix composition on the bonding environment and characteristics of Ag nanoparticles produced by gamma irradiation, Radiat. Phys. Chem. 202 (2023) 110564, https://doi.org/10.1016/j.radphyschem.2022.110564.
[62] R. Zein, I. Alghoraibi, C. Soukkarieh, M.T. Ismail, A. Alahmad, Influence of polyvinylpyrrolidone concentration on properties and anti-bacterial activity of green synthesized silver nanoparticles, Micromachines 13 (2022) 777, https://doi.org/10.3390/mi13050777.
[63] Z. Khan, S.A. Al-Thabaiti, A.Y. Obaid, A. Al-Youbi, Preparation and characterization of silver nanoparticles by chemical reduction method, Colloids Surf. B Biointerfaces 82 (2011) 513–517, https://doi.org/10.1016/j.colsurfb.2010.10.008.
[64] M.G. Kotp, A.F.M. EL-Mahdy, T.-L. Yang, S.-W. Kuo, A pyridinyl-phenanzine conjugated microporous polymer decorated with ultrafine Ag nanoparticles mediates the rapid reduction of nitrophenol, Microporous Mesoporous Mater. 331 (2022) 111669. DOI: 10.1016/j.micromeso.2021.111669.
[65] M.M. Ayad, W.A. Amer, M.G. Kotp, I.M. Minisy, A.F. Rehab, D. Kopecký, P. Fitl, Synthesis of silver-anchored polyaniline–chitosan magnetic nanocomposite: a smart system for catalysis, RSC Adv. 7 (2017) 18553–18560, https://doi.org/10.1039/C7RA02575K.
[66] Y. Han, X. Wu, X. Zhang, Z. Zhou, C. Lu, Reductant-free synthesis of silver nanoparticles-doped cellulose microgels for catalyzing and product separation, ACS Sustain. Chem. Eng. 4 (2016) 6322–6331, https://doi.org/10.1021/acssuschemeng.6b00889.
[67] Y.-P. Wu, G.-W. Xu, W.-W. Dong, J. Zhao, D.-S. Li, J. Zhang, X. Bu, Anionic lanthanide MOFs as a platform for iron-selective sensing, systematic color tuning, and efficient nanoparticle catalysis, Inorg. Chem. 56 (2017) 1402–1411, https://doi.org/10.1021/acs.inorgchem.6b02476.
[68] L. Miao, G. Liu, J. Wang, Ag-nanoparticle-bearing poly (vinylidene fluoride) nanofiber mats as janus filters for catalysis and separation, ACS Appl. Mater. Interfaces 11 (2019) 7397–7404, https://doi.org/10.1021/acsami.8b20759.
[69] M. Jeyapriya, B. Meenarathi, R. Anbarasan, Synthesis, characterization, catalytic and splinting activity of nano Ag end capped l-glutathione bridged amphiphilic diblock copolymer, J. Appl. Polym. Sci. 133 (2016) 43804, https://doi.org/10.1002/app.43804.
[70] N. Wang, F. Wang, F. Pan, S. Yu, D. Pan, Highly efficient silver catalyst supported by a spherical covalent organic framework for the continuous reduction of 4-nitrophenol, ACS Appl. Mater. Interfaces 13 (2021) 3209–3220, https://doi.org/10.1021/acsami.0c20444.
[71] Q. Yin, Q. Chen, L.-C. Lu, B.-H. Han, Sugar-based micro/mesoporous hypercross-linked polymers with in situ embedded silver nanoparticles for catalytic reduction, Beilstein J. Org. Chem. 13 (2017) 1212–1221, https://doi.org/10.3762/bjoc.13.120.
[72] M.M. Ayad, N.L. Torad, A.A. El-Nasr, W.A. Amer, Study on catalytic efficiency of platinum and silver nanoparticles confined in nanosized channels of a 3-D mesostructured silica, J. Porous Mater. 28 (2021) 65–79, https://doi.org/10.1007/s10934-020-00960-7.